Toward Quantitative Electrochemical Measurements on the Nanoscale by Scanning Probe Microscopy: Environmental and Current Spreading Effects

Thomas M. Arruda,[†,§] Amit Kumar,[†,⊥] Stephen Jesse,[†] Gabriel M. Veith,[‡] Alexander Tselev,[†] Arthur P. Baddorf,[†] Nina Balke,[†] and Sergei V. Kalinin[†,*]

[†]The Center for Nanophase Materials Sciences, Oak Ridge National Laboratory, Oak Ridge, Tennessee 37831, United States and [‡]Materials Science and Technology Division, Oak Ridge National Laboratory, Oak Ridge, Tennessee 37831, United States. [§]Present address: Department of Chemistry, Salve Regina University, Newport, RI, 02840, USA. [⊥]Present address: Centre for Nanostructured Media, Queen's University Belfast, Belfast BT7 1NN, United Kingdom.

ABSTRACT The application of electric bias across tip–surface junctions in scanning probe microscopy can readily induce surface and bulk electrochemical processes that can be further detected though changes in surface topography, Faradaic or conductive currents, or electromechanical strain responses. However, the basic factors controlling tip-induced electrochemical processes, including the relationship between applied tip bias and the thermodynamics of local processes, remains largely unexplored. Using the model Li-ion reduction reaction on the surface in Li-ion conducting glass ceramic, we explore the factors controlling Li-metal formation and find surprisingly strong effects of atmosphere and back electrode composition on the process. We find that reaction processes are highly dependent on the nature of the counter electrode and environmental conditions. Using a nondepleting Li counter electrode, Li particles could grow significantly larger and faster than a depleting counter electrode. Significant Li ion depletion leads to the inability for further Li reduction. Time studies suggest that Li diffusion replenishes the vacant sites after ~12 h. These studies suggest the feasibility of SPM-based quantitative electrochemical studies under proper environmental controls, extending the concepts of ultramicroelectrodes to the single-digit nanometer scale.

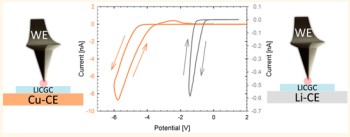

KEYWORDS: scanning probe microscopy · solid state electrolyte · counter electrode effects · Li ion battery · nanoscale electrochemistry

Energy storage and conversion,[1,2] electroresistive nonvolatile memories for information storage,[3–5] corrosion of metals and alloys and fatigue of oxide-based electronic devices[6] are but a few examples of electrochemical transformations in solids. In many cases, the functionality of these systems are controlled by nanoscale phenomena, such as nucleation sites for new phase formation in energy storage systems, conductive filaments in memristors, or pits in corrosion. Correspondingly, understanding the mechanisms of these processes necessitates probing local electrochemical functionalities on localized, ideally single-nanometer and subnanometer length scales.

The application of electric bias across tip–surface junctions in scanning probe microscopy can readily induce surface and bulk electrochemical processes at selected locations on sample surface. In fact, the role of electrochemical reaction currents (Faradaic) in scanning tunneling microscopy was recognized since early days of scanning probe microscopy (SPM).[7] Subsequently, multiple groups explored voltage-based nanofabrication in which conductive tips induce local electrochemical processes such as nanooxidation of metals and semiconductors,[8,9] deposition of carbon and semiconductors,[10] and local reduction of ionic conductors and formation of metallic nanostructures.[11–13] In some cases, high electric fields at the tip–surface junctions and nanoscale localization of the reaction zone(s) enable unusual electrochemical processes such as the formation of SiC from SiO_2 and hexane or splitting of CO_2,[10] opening a pathway for exploring high-energy electrochemical processes.

The onset and progression of electrochemical processes at the tip–surface junction can be detected though dynamic changes

* Address correspondence to Sergei2@ornl.gov.

Received for review July 8, 2013 and accepted August 22, 2013.

Published online August 22, 2013
10.1021/nn4034772

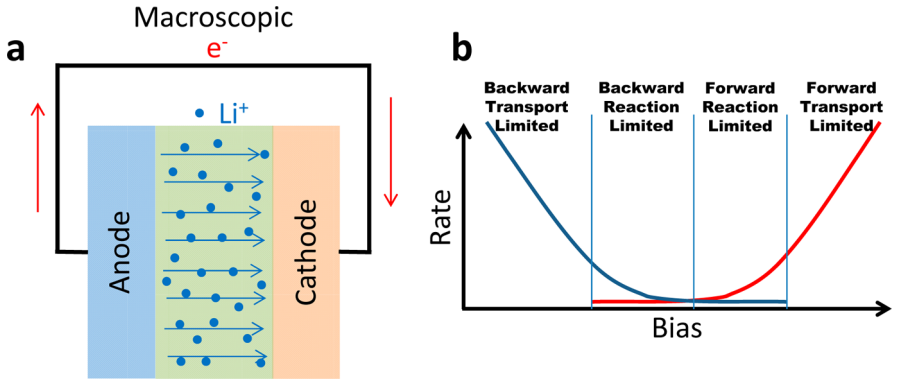

Figure 1. (a) Illustration of electronic and ionic transport on the macroscopic level and (b) general description of the influence of bias on reaction rate as it pertains to transport and reaction product.

in surface topography,[14] direct detection of Faradaic or monitoring changes in conductive currents, or electromechanical response.[15−17] Performing these measurements as a function of position on sample surface then provides spatial maps of local electrochemical activity that can be further related to local structure, presence of structural and morphological defects, and other inhomogeneities on sample surface. Hence, SPM can be envisioned as universal tool for probing local electrochemical activity, extending the concept of ultramicroelectrodes to spatially resolved imaging and enabling electrochemical probing on the level of a single defect. However, the systematic study of local electrochemical phenomena by SPM requires quantitative understanding of the factors controlling tip-induced processes to relate the tip bias to local shifts in the electrochemical potential driving the reaction(s). Only then can parameters such as local nucleation voltage probed by SPM be related to the thermodynamics of the electrochemical process.

Here, we explore the factors controlling tip-induced electrochemical reactions using Li-ion reduction on a lithium ion conducting glass-ceramic (LICGC) as a model system, the spatial localization of the cathodic process, and the role of ionic and electronic transport. We demonstrate that quantitative information on the local overpotentials for second phase formation can be obtained if the proper electrochemical environment is established. These studies suggest the feasibility of SPM-based quantitative electrochemical studies under proper environmental controls, extending the concepts of ultramicroelectrodes to the single-digit nanometer scale.

RESULTS AND DISCUSSION

Macroscopic *versus* Local Electrochemistry. To illustrate the scope of the problems we aim to explore, Figure 1 illustrates the schematic diagrams of the electrochemical process in the macroscopic systems with planar electrodes. In this case, the application of the sufficiently high electric bias between two electrodes separated by Li-ion electrolyte will result in Li-ion motion to the cathode and reduce to form Li metal *via* the reaction (note potentials are *vs* standard hydrogen electrode [SHE]):

$$Li^+ + e^- \rightarrow Li_{(s)},\ E^0 = -3.04\ V\ vs\ SHE \qquad (1)$$

The anode process depends on the nature of the anode, and for the electroplating process (Li anode) can be the reverse of eq 1, whereas for a blocking anode, the reaction can be oxidation of the current collector:

$$Cu \rightarrow Cu^{+/2+} + 1 \text{ or } 2e^-$$

$$E^0 = -0.521,\ -0.342\ V\ \ vs\ SHE \qquad (2)$$

or oxygen evolution reaction $2\ O^{2-} \rightarrow O_2 + 4\ e^-$ (*e.g.*, from lattice oxygen). The total process will then be a sum of cathodic and anodic half-reactions, with total voltage being determined by the sum of the thermodynamic potentials and overpotentials for both half reactions and potential drop (defined hereafter as IR) for ionic transport between the cathode and anode. Overall, mass and charge conservation laws must be satisfied both locally and globally.

The process becomes thermodynamically possible when the applied bias exceeds thermodynamic potential defined by both half-reactions (note that strictly speaking for below this potential inverse reaction should proceed, if the product is available). For example, for Li formation on the two blocking electrodes the process is close to that of Li_2O reduction. However, at this voltage the rate is zero, and finite rate requires excess potential to compensate for electrode polarization. On subsequent increases of applied bias, the process accelerates until at some point it becomes limited by mass transport. In this regime, the potential drops both at the electrodes and the bulk. These stages and voltage dependence of electrochemical process rates are well explored in the context of bulk electrochemistry.[18]

We note that the same factors are relevant in tip-induced electrochemical processes, and in particular, mass and charge conservation should be maintained.

However, in SPM (a) reaction zones are smaller, with spatial confinement effects leading to larger overpotentials, (b) the local contact areas are much smaller, and hence IR drops can be much larger, but (c) the availability of free surface makes contribution of stray counter reactions more significant.

In general, the critical bias can be written as

$$U = V_t + \eta_t + V_c + \eta_c + \mathrm{IR} \quad (3)$$

where V_t and V_c are thermodynamic potentials for the tip and counter reactions, η_t and η_c are the corresponding overpotentials, and IR is the ionic transport resistance term. For localized tip-induced processes, V_t, η_t and IR are expected to be strong functions of tip position, with V_t and η_c being controlled bulk thermodynamics and surface properties of the material, respectively, and IR is the sum ionic and contact resistances. At the same time, V_c and η_c are not position dependent for delocalized counter-reaction. We also note that V_t and V_c can usually be estimated (within 10−100 mV) from the corresponding bulk thermodynamic values, η_t and η_c are unlikely to exceed ~1 V, whereas IRs are dependent on many other factors (*e.g.*, electrolyte thickness, conductivity, temperature *etc.*).

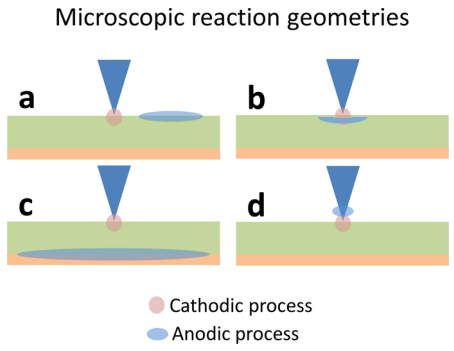

Figure 2. Reaction scheme possibilities on the nanoscale. Note the cathodic reaction always occurs directly under the tip, whereas the anodic process progresses near the reaction zone (a), all around the reaction zone (b), at the counter electrode (c), or on the tip (d).

Note that uncertainty in the counteraction makes the IR effect difficult to estimate since the localization of the counter-reaction zone is not necessarily known and strongly depends on the relative ionic and electronic conductivity of the material and (necessarily) its surface and availability of stray reaction processes. Some of the possible localization of the cathodic and anodic processes in SPM experiments are illustrated in Figure 2. However, in virtually all SPM-based electrochemical studies to date, only the processes on the tip−surface junction were analyzed, while the nature and localization of counter-reaction was ignored. Here, we systematically explore the effects of counter-reaction and IR drops on the Li nanoparticle formation on the LICGC surface.

Effects of Local Counter-Electrode. To explore the role of localization of cathode and anode processes, we explore the tip-induced reduction of Li on the LICGC surface. This material is well-explored in the context of Li-air batteries, and in particular offers high surface stability in contact with air and water and high ionic conduction at room temperature. The local reduction of Li on this surface has been extensively studied by Arruda *et al.*,[12,13] Kumar *et al.*,[19] and Kruempelmann *et al.*[20,21]

A typical example of the tip-induced electrochemical Li reduction for a LICGC sample on a Cu bottom electrode is illustrated in Figure 3. Here, the triangular waveform is applied over a rectangular grid of points (10 × 10) on the pristine LICGC surface (Figure 3a), resulting in the formation of metallic Li nanoparticles,

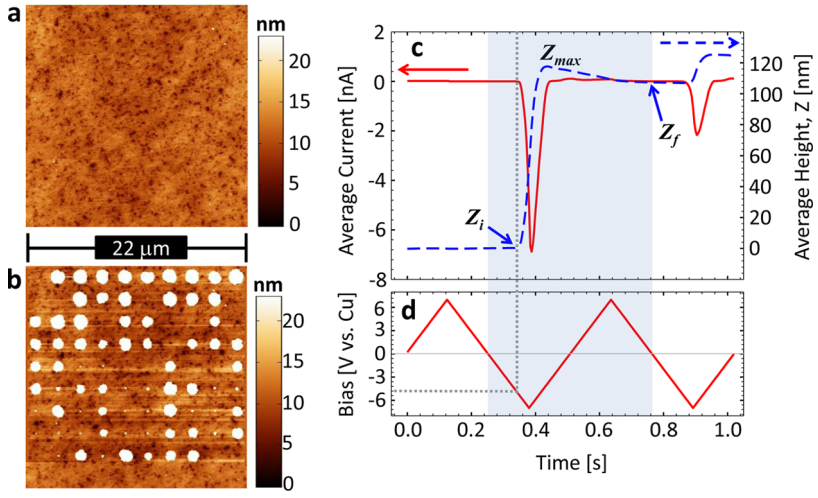

Figure 3. (a) Pristine surface topography of the LICGC surface and (b) topography after application of triangular voltage sweep on a rectangular grid. Note the significant variations in the Li particle size related to variability of local electrochemical reactivity of the surface. (c) Current and surface displacement during the application of voltage waveform shown in (d). Note the shaded area in (c) and (d) represents the expected response for one cycle beginning with the cathodic scan first. The values Z_i, Z_{max}, and Z_f represent the initial height, maximum height, and final height, which are used to compute the height reversibility.

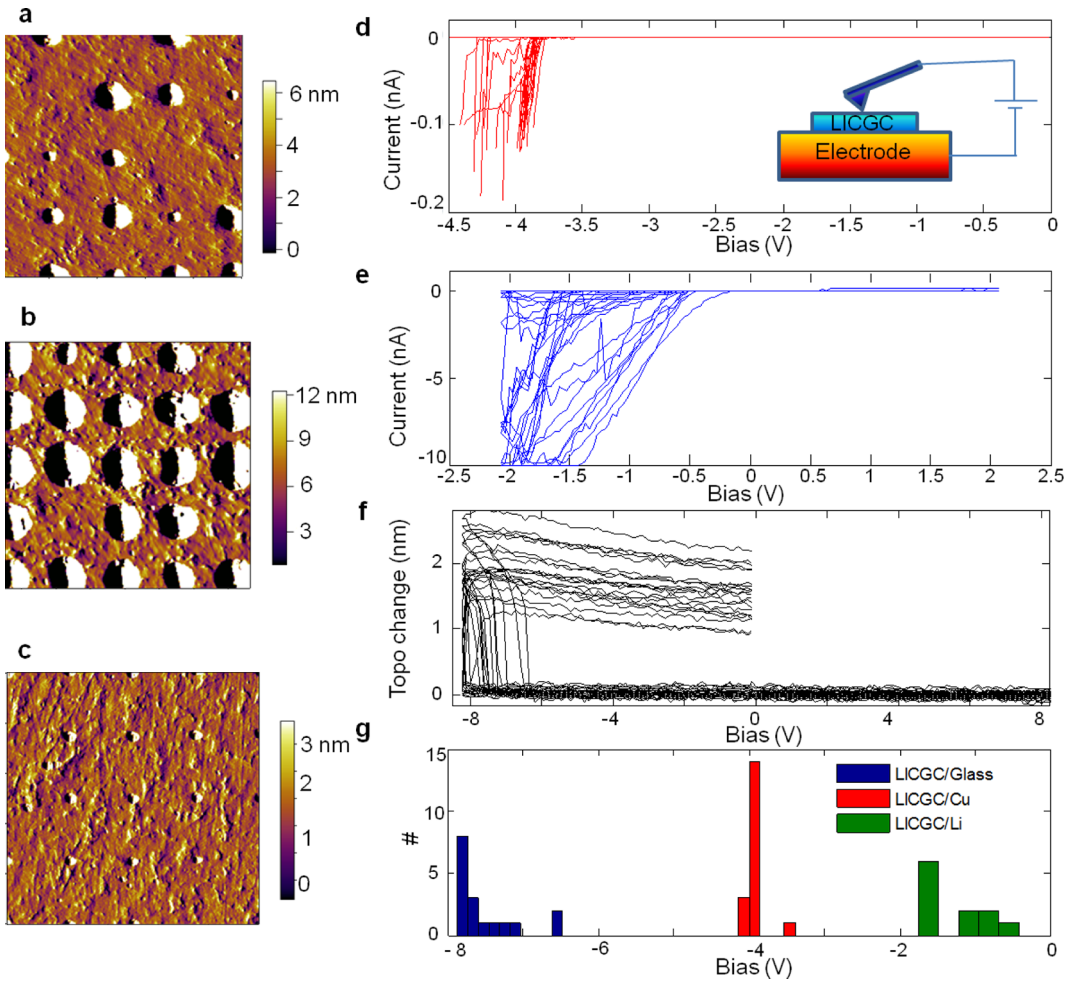

Figure 4. Topography of LICGC surface after electrochemical reduction was performed with (a) Cu, (b) Li, and (c) glass counter-electrodes. Corresponding *I*−*V* behavior for the shown points is shown for (d) Cu electrode, (e) Li electrode, and *Z*−*V* behavior for (f) glass as counter-electrode. The experimental setup is shown as an inset in (d) for different choice of electrodes. (g) Distributions of the nucleation biases for different counter-electrodes.

and allowing both cathodic and anodic processes to be explored. The broad distribution of Li particle sizes is clearly visible in Figure 3b, and is related to the strong variability of the electrochemical activity of the surface; which in turn can be related to variations in local overpotentials, ionic conductivity, or thermodynamic reduction potentials in eq 3.

The evolution of the current and tip displacement during application of the triangular voltage waveform is shown in Figure 3c,d. The onset of Li-reduction is associated with the concurrent onset of (Faradaic) current flow and tip deflection due to Li particle formation. Note that the critical bias corresponding to the formation of Li nanoparticles is ∼−4 V at this location. Additionally, the process is largely irreversible, with only partial height relaxation and very small anodic currents observed. On the repeated application of the waveform, the subsequent growth of particle is observed at virtually the same bias. For measurements at multiple locations, the lowest value that defines initiation of reduction process in the most active regions is −3.35 V, and compares favorably to the potential of Li reduction from eq 1 (∼3.04 V).

To explore the role of the anodic process, the measurements were performed using a Cu counter electrode, Li-metal counter electrode, and glass counter electrode, and the corresponding results are illustrated in Figure 4. On the Cu counter electrode, the Li particle are nucleated between ∼3 and 4 V and rapidly grow after nucleation, corresponding to very sharp upturn of the *I*−*V* curve. The distribution of the nucleation biases is relatively high, as is the particle size distribution in the end of bias sweep (no feedback on limiting current or deflection). Note that the average nucleation potential can be correlated with the average electrochemical activity of the surface in an SPM experiment. However, for comparison with bulk reactivity, the relevant parameter is the low-bias tail of this distribution (with necessarily limited sampling), since it represents the bias required to create Li nanoparticles at the most active sites on the surface. These sites will then serve as the nucleation sites from which the growth will proceed.

In comparison, experiments that employ a Li counter electrode exhibit a nucleation potential of ∼0.5 V

on average. The resulting particles are significantly larger, indicating that Li^+ replenishment from the Li foil may diminish any adverse concentration depletion effects. For example, in the case of the Cu counter-electrode, Li is extracted from LICGC and not replaced (at least not replaced by Li^+). This may lead to IR losses that will decrease mass transport of Li^+ to the reaction zone, hence resulting in smaller particles. More discussion on Li depletion is provided in a section below. It is also worth noting that this cell configuration, despite being a two-electrode setup, can be reasonably described employing a Li reference electrode since the area of the Li foil far exceeds that of the deposited particles. Thus, the potentials measured for the reaction onset directly represent the overpotential required for Li deposition to occur.

Finally, on the glass substrate, the nucleation process is strongly suppressed, and current cannot be measured due to the insulating (electrons) nature of glass. However, the nucleation voltages can still be determined using strain spectroscopy ($Z-V$ curve), as shown in Figure 4f. Notice the nucleation potential is high (6−8 V) in comparison to the Li and Cu electrodes. Additionally, the total particle height is on the order of 2 to 3 nm, in comparison to unlimited (>100 nm) growth for the Li and Cu counter-electrodes. This suggests that sufficiently high voltages can indeed nucleate particles, but sustained particle growth is impossible without having a counter reaction present. Thus, any counter reaction that *does* occur to facilitate this particle nucleation must be local (*i.e.*, Figure 2, all except (c)) such as proton injection from chemisorbed H_2O, *etc.* Notably, somewhat similar behavior is observed using a Cu counter electrode without a silver paint connection to LICGC is used, thus preventing adequate electrical contact.

We further discuss the thermodynamics of tip-induced nucleation processes in more detail. The thermodynamic potential for the reduction of Li from Li_2O is −3.04 V. While the activity of Li_2O in LICGC can deviate from unity, the close chemical similarity between the two suggest that such deviation is minimal, while an order of magnitude change in activity changes the thermodynamic reduction by ∼27 mV. The measured nucleation potentials (−3.7 ± 0.5 V in these data) hence provide a sum of intrinsic thermodynamic potential, overpotential for particle formation (local nucleation barrier for particle formation in the tip field), and ohmic (IR) drop in the material. For the Li electrode, the reduction potential is shifted to −0.5 ± 0.1 V, suggesting that this value corresponds to the sum of nucleation potential and IR drop. Remarkably, this profound difference is observed despite the fact that the anode is both much larger than the tip−surface junction and is separated by macroscopic (fraction of mm) distances.

Finally, it is worth noting that the total cell potential for the glavanostatic, two electrode process is described by

$$E_{cell} = E_{ca} - E_{an} \quad (4)$$

where E_{cell} is the total cell potential driven, E_{ca} is the cathode potential, and E_{an} is the anode potential. In this case, E_{ca} and E_{an} can be described by eqs 1 and 2, respectively, and E_{cell} can reasonably be expected to be ∼2.5 − 2.8 V. Note the potentials observed in the experimental data manifest near ∼3.5 V suggesting the differences observed between expected and observed values reflect the combined overpotentials for E_{ca} and E_{an}.

Effect of Water Adlayer. We further explore the role of environmental conditions in tip-induced electrochemical processes with a poorly defined counter electrode. The reaction thermodynamics is affected by oxygen partial pressure, with the direction of the shift determined by LeChatelier's principle so that reduction of partial pressure of oxygen facilitates reduction, shifting the reduction potential to less negative values. However, the electrochemical behavior can also be affected by the presence of a water layer, that can both catalyze the complementary anodic reaction and allow for increased electronic/ionic conduction, as illustrated in Figure 1. However, note that mere presence of water is insufficient to induce alternative electrochemical processes, since charge conservation requires additional charge carriers (electrons or protons).

Shown in Figure 5 is the evolution of the character of Li particle formation on LICGC in an Ar filled glovebox on the glass electrode. In this case, the absence of a well-defined electronic conductive path suggests that the counter-reaction process is oxygen evolution (likely from the water adlayer rather than LICGC matrix) and IR process is controlled by the ionic/electronic transport through conductive water layers on the surface. Note the pronounced difference in reduction *vs* time in the glovebox. The onset of nucleation shifts to progressively higher voltages for longer exposures to dry, oxygen void glovebox atmosphere. Immediately after introduction to glovebox, the reaction is observed at ∼2 V bias. In 2 h, there is no reaction at 2 V, but current can be observed when the bias is increased to ∼5 V. After 24 h, 5 V is insufficient to cause particle formation and biases of ∼8 V is required for reaction. In all cases, the reaction process is self-limiting (unlike rapid takeoff of strain curves for well-defined counter electrode) due to the relatively little amount of counter reactants available. Even the application of 50 V bias does not create micrometer-scale particles, whereas in ambient conditions, >10 μm particles form under these conditions. We ascribe this behavior to the slow evaporation of physisorbed water layers, that results in the progressive increase of the IR term in eq 3 (since the local overpotential should not be affected, and

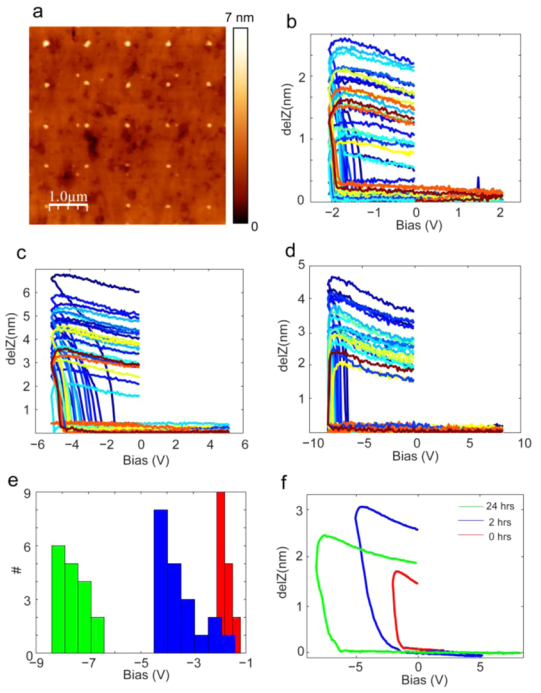

Figure 5. Atmospheric effect on Li-particle formation. Shown are Li-particle morphologies formed (a) 2 h after introduction of LICGC sample in the glovebox; (b–d) corresponding strain–voltage curves; (e) histogram of nucleation biases; (f) corresponding average curves.

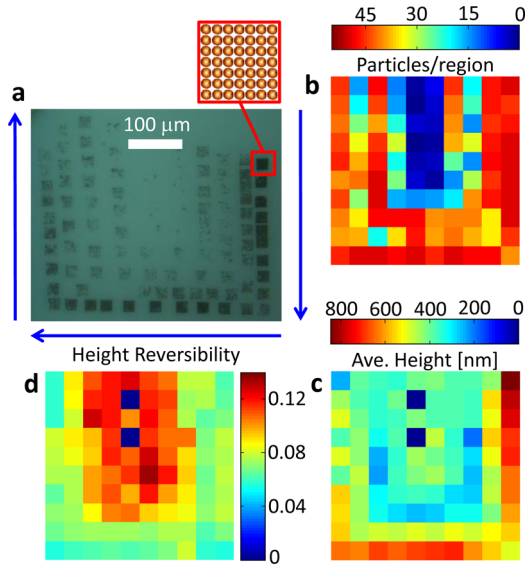

Figure 6. (a) Optical micrograph of the area formed with multiple grid writing experiments. The inset shows the grid used in all cases (7 × 7 over 20 μm). The writing was performed in a sequence of concentric U-shapes. Evolution of (b) number of particles per grid, (c) average particle height within the region, and (d) average particle height reversibility. In all cases, the particles were generated using a cyclic voltammogram waveform (±15 V window, ~58 V s^{-1}), and with the use of a Cu counter electrode, currents and height changes were measured simultaneously.

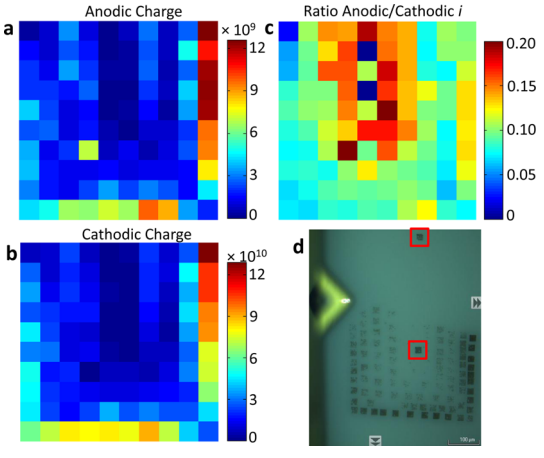

Figure 7. (a) Average anodic charge transferred per region (shown in number of electrons transferred), (b) average cathodic charge transferred per region, (c) ratio of anodic to cathodic charge transferred, and (d) optical image of the entire array of regions taken ~12 h after the experiment completed.

thermodynamic potential can only decrease in the oxygen-poor environment).

Depletion Effects and IR Drop. We further aim to explore the effect of ionic conduction. Macroscopically, the IR effects can be explored though the variation of the system size, linearly coupled to the total resistance. However, for a tip-electrode the local spreading resistance is controlled by the tip–surface contact radius, and hence, the variations in local ionic conductance below the tip are expected to dominate the signal.

To explore the Li^+ depletion effects, we have generated arrays of very large particle over 20 μm regions of the surface, with the arrays roughly arranged in the form of concentric U-shapes as shown in Figure 6a. In this case the outer regions predominantly exhibit large particles in the 7 × 7 arrays, with most of the regions producing 49 particles per array (Figure 6b). However, the inner regions appear to exhibit fewer particles per array, and in the case of the two innermost regions, almost no particles were able to be formed. A summary of the charge transferred is provided in Figure 7a–c. Notably, the largest currents (both anodic and cathodic) were observed around the "fringe" where the particles were large and plentiful (Figure 6b,c). This suggests the fringe area was not yet Li^+ depleted, and thus, the reaction could progress with considerable ease. At the same time, the reversibility was *highest* for the particles generated in the depleted region. This indicates that it is easier to reoxidize the particles back into LICGC matrix when the region is depleted, facilitating the reincorporation of Li ions into the LICGC matrix.

Interestingly, when the measurements were performed in the depleted zone ~12 h later, particle formation ensued with the same ease that was observed for the fringe areas (Figure 7d), suggesting that Li ions from distant regions of the sample diffuse into the depletion area restoring its original reactivity. We further note that these depletion effects are observed only when the macroscopically large volumes of Li are

generated. Their effect on local measurements can be established based on systematic changes in particle sizes across the arrays, and it was not observed in other experiments reported here. Thus, we suggest that the formation of small (~1 μm and below) particles in relatively small arrays (10 × 10) do not cause any major depletion effects.

CONCLUSIONS/SUMMARY

To summarize, we have systematically explored the role of the counter-reaction, ionic transport, and environment on the tip-induced electrochemical phenomena in the model LICGC system. For local electrochemical measurements, similarly to macroscopic analogs, the second half reaction can be the limiting stage. In the specific case studied here, the presence of a Li anode separated by several hundred micrometers from the tip surface junction shifts the nucleation reaction bias for nanometer scale Li particles from −4 to ~−0.5. V. This shift is sensitively affected by stray surface transport and electrochemical reactions, and dependent on the environmental conditions that can allow stray reactions that can dominate the system behavior. Furthermore, although depletion effects can be observed, they are unlikely to affect process when minute quantities of reaction product are generated.

The voltage required to induce tip−surface reaction has contributions from local thermodynamics, overpotential for nucleation, IR drop, and both thermodynamic and kinetic parameters of the counter-reactions. For cases when ionic conductivity of the material is high, corresponding spreading resistances are low, and counter-reaction is well identified and has low relative impedance, the measured nucleation potential is a quantitative measure of the local electrochemical activity of the surface that can then be mapped with high spatial resolution.

For low ionic conductivity, but well-defined counter-reaction, the measured nucleation biases will largely represent the variation of local diffusion through the spreading ionic resistances. Finally, for poorly defined counter-reactions, the quantitative interpretation is very challenging and the process will be controlled by stray reaction processes. These considerations suggest that SPM-based electrochemical studies can be quantitative, but necessitate precise control of electrochemical environment including both atmosphere and localization site for counter-reaction.

Overall, these studies demonstrate not only the guidelines for quantitative electrochemical measurements on the nanoscale that can be employed to understand internal functionality of fuel cells, batteries, and memristors, but also the structure-electrochemical property relationships on a single defect level, establishing the bridge between materials functionality and theory.

MATERIALS AND METHODS

Lithium ion conducting glass ceramic (AG01, 150 μm thick 1 in.^{2} plate) was purchased from Ohara, Inc. AFM tips employed were Cr/Pt (5/25 nm thick) coated Budget Sensors (Multi 75E-g, k = 3 N m^{-1}). In all cases, the AFM tip served as the working electrode and the counter electrode was as described above. In the case of the Cu electrode, an Ag based adhesive (Ted Pella) was employed for good electrical contact. In the case of the Li foil counter electrode, a 1 μm layer of lithium phosphorus oxynitride (LiPON) was applied (magnetron sputtering)[22] between LICGC and Li to prevent decay of LICGC. Cyclic voltammetry waveforms were generated using a National Instruments arbitrary waveform generator (NI 5412/5122) in conjunction with a Femto DLPCA-200 variable gain current amplifier with an amplification gain typically 10^8 V/A. The system was implemented on an Asylum Research Cypher model AFM contained inside of an Ar filled glovebox.

Conflict of Interest: The authors declare no competing financial interest.

Acknowledgment. This research was conducted at the Center for Nanophase Materials Sciences, which is sponsored at Oak Ridge National Laboratory by the Scientific User Facilities Division, Office of Basic Energy Sciences, U.S. Department of Energy. The authors gratefully acknowledge Roger De Souza (RTW Aachen) for thought-provoking discussions that led to this work and Nick Lavrick (CNMS) for eminently useful references on the role of ionic dynamics on surface conductance on dielectrics.

REFERENCES AND NOTES

1. Minh, N. Q. Ceramic Fuel-Cells. *J. Am. Ceram. Soc.* **1993**, *76*, 563–588.
2. Bagotsky, V. S. *Fuel Cells: Problems and Solutions*; Wiley: Hoboken, NJ, 2009.
3. Waser, R. *Nanoelectronics and Information Technology*, 3rd ed.; Wiley: Weinheim, Germany, 2012.
4. Valov, I.; Waser, R.; Jameson, J. R.; Kozicki, M. N. Electrochemical Metallization Memories-Fundamentals, Applications, Prospects. *Nanotechnology* **2011**, *22*, 254003.
5. Sawa, A. Resistive Switching in Transition Metal Oxides. *Mater. Today* **2008**, *11*, 28–36.
6. Tagantsev, A. K.; Stolichnov, I.; Colla, E. L.; Setter, N. Polarization Fatigue in Ferroelectric Films: Basic Experimental Findings, Phenomenological Scenarios, and Microscopic Features. *J. Appl. Phys.* **2001**, *90*, 1387–1402.
7. Fan, F. R. F.; Bard, A. J. STM on Wet Insulators—Electrochemistry or Tunneling. *Science* **1995**, *270*, 1849–1851.
8. Tello, M.; Garcia, R. Nano-Oxidation of Silicon Surfaces: Comparison of Noncontact and Contact Atomic-Force Microscopy Methods. *Appl. Phys. Lett.* **2001**, *79*, 424–426.
9. Garcia, R.; Calleja, M.; Perez-Murano, F. Local Oxidation of Silicon Surfaces by Dynamic Force Microscopy: Nanofabrication and Water Bridge Formation. *Appl. Phys. Lett.* **1998**, *72*, 2295–2297.
10. Garcia, R.; Losilla, N. S.; Martinez, J.; Martinez, R. V.; Palomares, F. J.; Huttel, Y.; Calvaresi, M.; Zerbetto, F. Nanopatterning of Carbonaceous Structures by Field-Induced Carbon Dioxide Splitting With a Force Microscope. *Appl. Phys. Lett.* **2010**, *96*, 143110–3.
11. Lee, M.; O'Hayre, R.; Prinz, F. B.; Gur, T. M. Electrochemical Nanopatterning of Ag on Solid-State Ionic Conductor $RbAg_4I_5$ Using Atomic Force Microscopy. *Appl. Phys. Lett.* **2004**, *85*, 3552–3554.
12. Arruda, T. M.; Kumar, A.; Kalinin, S. V.; Jesse, S. Mapping Irreversible Electrochemical Processes on the Nanoscale:

Ionic Phenomena in Li Ion Conductive Glass Ceramics. *Nano Lett.* **2011**, *11*, 4161–4167.
13. Arruda, T. M.; Kumar, A.; Kalinin, S. V.; Jesse, S. The Partially Reversible Formation of Li-Metal Particles on a Solid Li Electrolyte: Applications toward Nanobatteries. *Nanotechnology* **2012**, *23*, 325402–9.
14. Tian, Y.; Timmons, A.; Dahn, J. R. *In Situ* AFM Measurements of the Expansion of Nanostructured Sn-Co-C Films Reacting with Lithium. *J. Electrochem. Soc.* **2009**, *156*, A187–A191.
15. Balke, N.; Jesse, S.; Morozovska, A. N.; Eliseev, E.; Chung, D. W.; Kim, Y.; Adamczyk, L.; Garcia, R. E.; Dudney, N.; Kalinin, S. V. Nanoscale Mapping of Ion Diffusion in a Lithium-Ion Battery Cathode. *Nat. Nanotechnol.* **2010**, *5*, 749–754.
16. Balke, N.; Jesse, S.; Kim, Y.; Adamczyk, L.; Tselev, A.; Ivanov, I. N.; Dudney, N. J.; Kalinin, S. V. Real Space Mapping of Li-Ion Transport in Amorphous Si Anodes with Nanometer Resolution. *Nano Lett.* **2010**, *10*, 3420–3425.
17. Kumar, A.; Ciucci, F.; Morozovska, A. N.; Kalinin, S. V.; Jesse, S. Measuring Oxygen Reduction/Evolution Reactions on the Nanoscale. *Nat. Chem.* **2011**, *3*, 707–713.
18. Bard, A. J.; Faulkner, L. R. *Electrochemical Methods: Fundamentals and Applications*, 2nd ed.; Wiley: New York, 2001.
19. Kumar, A.; Arruda, T. M.; Tselev, A.; Ivanov, I. N.; Lawton, J. S.; Zawodzinski, T. A.; Butyaev, O.; Zayats, S.; Jesse, S.; Kalinin, S. V. Nanometer-Scale Mapping of Irreversible Electrochemical Nucleation Processes on Solid Li-Ion Electrolytes. *Sci. Rep.* **2013**, *3*, 1621–1629.
20. Kruempelmann, J.; Reinhardt, H.; Yada, C.; Rosciano, F.; Hampp, N.; Roling, B. AFM Tip-Induced Metal Particle Formation on Laser-Structured and on Unstructured Surfaces of Solid-State Ion Conductors. *Solid State Ionics* **2013**, *234*, 46–50.
21. Kruempelmann, J.; Dietzel, D.; Schirmeisen, A.; Yada, C.; Rosciano, F.; Roling, B. Nanoscale Electrochemical Measurements on a Lithium-Ion Conducting Glass Ceramic: *In Situ* Monitoring of the Lithium Particle Growth. *Electrochem. Commun.* **2012**, *18*, 74–77.
22. Lu, Y. C.; Crumlin, E. J.; Veith, G. M.; Harding, J. R.; Mutoro, E.; Baggetto, L.; Dudney, N. J.; Liu, Z.; Shao-Horn, Y. *In Situ* Ambient Pressure X-ray Photoelectron Spectroscopy Studies of Lithium-Oxygen Redox Reactions. *Sci. Rep.* **2012**, *2*, 715–721.